Additive Manufacturing 22 (2018) 343–350

Contents lists available at ScienceDirect

Additive Manufacturing

journal homepage: www.elsevier.com/locate/addma

Full Length Article

Direct write fabrication of high-density parallel silver interconnects

Alan Shen[a], Dustin Caldwell[c], Anson W.K. Ma[a,b], Sameh Dardona[c,*]

[a] Department of Chemical and Biomolecular Engineering, University of Connecticut, Storrs, CT, 06269, USA
[b] Polymer Program, Institute of Materials Science, University of Connecticut, Storrs, CT, 06269, USA
[c] Physical Sciences Department, United Technologies Research Center, East Hartford, CT, 06118, USA

ARTICLE INFO

Keywords:
Direct write
Interconnects
Rheology
Wear sensor
Printed electronics
Ink dispensing
Narrow interconnects

ABSTRACT

This study investigates the suitability of direct write (DW) technology for the fabrication of high-resolution wear sensors. We demonstrate the production of high-density parallel interconnect traces and provide recommendations for processing conditions to minimize line width and line spacing based on DW ink rheology. To create parallel silver lines with 50 μm center-to-center spacing and 15 μm line width on alumina substrates, we used an nScrypt DW system and sintered the lines at 625 °C in air. The sintered lines exhibited an electrical resistivity of 5.29×10^{-8} Ω m (about three times bulk silver resistivity reported in the literature) with a standard deviation of 3.68×10^{-9} Ω m (ca. 7% variation). To determine the conditions needed to consistently create fine conductive lines, we simulated the volumetric flow rate and analyzed the effects on line geometry of several printing parameters including valve opening, dispensing gap, and substrate translation speed. Our results indicate decreasing the valve opening, decreasing the dispensing gap, and/or increasing the translation speed of the substrate reduces the resultant printing flow rate and cross-sectional area of DW lines. For a fixed valve opening and dispensing gap, we also observed broken lines due to overstretching of the inks at exceedingly high substrate translation speeds.

1. Introduction

Many industrial applications require sensors to monitor wear of components. In any industrial application with two or more components in physical contact, relative rotation or translation motion between the components can result in excessive wear of the surface or top coating [1] Such wear can eventually affect the performance of the components, system, or assembly. Various approaches aim to control the amount of wear within acceptable limits: for example, via use of lubricants or via material or design specifications. Applications that require relative motion to perform (e.g., brake linings, gears, and sliders) must monitor inevitable wear of components for risks to performance. Current strategies to monitor the health and usability of components include wear indicators [2] and inspection, the latter often proving infeasible due to, e.g., time, labor, cost, and down time disruptions. The myriad industrial applications in which component wear must be monitored means high demand for wear sensors that can be embedded without removing components from their operational positions. Typical design for an embedded, wear-monitoring system employs a circuit with narrow, closely spaced conductive leads deployed near the surface and connected to a set of parallel resistors (Fig. 1). Wear due to relative motion progressively removes material, cutting the conductive leads in succession. Removal of each conductive lead increases total resistance and thus changes the measured voltage. The sensitivity of a sensor of this design correlates with the size and spacing of the conductive leads: the thinner the line width and narrower the line-to-line spacing (center-to-center spacing between two adjacent interconnect traces), the higher the resolution of a sensor.

Direct Writing (DW) offers an attractive method for manufacturing wear sensors of this design. An additive manufacturing (AM) technique, DW enables direct deposition of electronic components and functional or structural patterns using different materials, without masks or subsequent etching processes [3–8]. The literature distinguishes three types of DW according to dispensing mechanisms: extrusion-based DW, e.g. robocasting; droplet-based DW, e.g. inkjet and aerosol jet dispensing; and laser DW [3,9]. Our study employs extrusion-based DW, in which a software-guided machine extrudes continuous filaments onto a substrate through a nozzle. Following deposition, heat treatment (e.g., curing or sintering) endows the deposited material with the properties needed to achieve its full performance. DW enables the fabrication of sensing devices conformal to the product surface or embedded within the product structure [10]. Such additive processes minimize material waste and tooling requirements and speed processing time. Further, use of DW for electronics prototyping and possibly manufacturing

* Corresponding author.
E-mail address: dardona@utrc.utc.com (S. Dardona).

https://doi.org/10.1016/j.addma.2018.05.010
Received 20 June 2017; Received in revised form 18 October 2017; Accepted 6 May 2018
Available online 17 May 2018

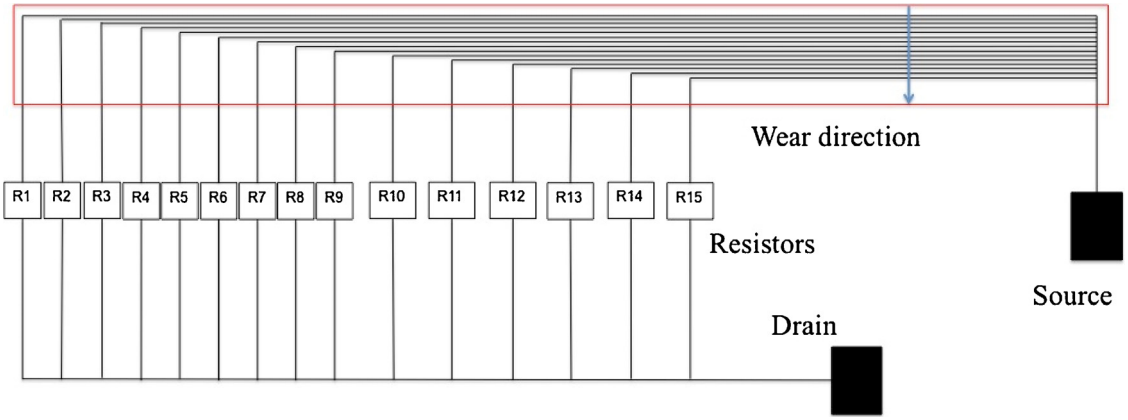

Fig. 1. Schematic diagram of a wear sensor design, in which the conductive interconnects (in red box) are fabricated by extrusion-based direct write (DW) method. As wear occurs, the conductive interconnects are progressively removed in the direction of wear, leading to step changes in resistance. The resolution of this sensor design depends on the line width and line-to-line spacing of the interconnects. (For interpretation of the references to colour in this figure legend, the reader is referred to the web version of this article).

eliminates the photolithography masking and etching steps in conventional electronics fabrication.

Other common methods for creating conductive traces directly include screen-printing and inkjet and aerosol jet printing. Screen-printing requires an upfront investment in a stencil, which requires regular cleaning and lacks versatility when it comes to design changes. Moreover, the spatial resolution for screen-printing is generally much lower than more expensive photolithography methods capable of producing patterns with line width and line spacing on the order of 10 nm. To achieve high-resolution patterning with screen-printing, Hyun et al. reported a line width of 40 μm using graphene ink and silicon stencils [11]. The primary limiter of resolution for screen-printing is the open area of the stencil, and printing features less than 40 μm proves challenging due to ink bleeding [12]. Inkjet [13] and aerosol jet printing [14] can produce conductive traces with a line width on the order of 50 μm and even 10 μm; however, these techniques require a low viscosity ink (typically less than 50 cP), which further limits the solid loading (content of conductive material) in the ink (< 20%) [12] After the carrier solvent is removed, a single-pass printing usually results in sub-micron thick layers with relatively high resistance due to the small cross-sectional area [15]. Low resistance is desirable, because high conductivity enables high accuracy and reliability of sensors. Multiple passes can increase thickness and reduce resistance of the conductive traces, but the additional processing time and imperfect layer-to-layer registration compromise both throughput and resolution.

Given its advantages, extrusion-based DW technology offers a promising method to produce high-resolution wear sensors. Currently, Li et al. [16] report the smallest line width and line-to-line spacing achieved by extrusion-based DW technology: 25 μm and 100 μm, respectively. Similarly, Wei et al. employed extrusion-based DW[10] to fabricate carbon-based resistive strain gauge sensors with a 175-μm line width and 0.5-mm line-to-line spacing on titanium substrate. Palmer [17] and Perez et al. [18] report extrusion-based DW of interconnects for integrated electronics, and Lewis et al. [19,20] and Dimos et al. [21,22] investigated the influence of ink rheology on line resolution and surface topography of printed material for extrusion-based DW. Their studies suggest the apparent viscosities at low shear rates (< 1 s^{-1}) strongly influence the line widths (resolution) and surface topographies. For instance, pastes with a higher viscosity at low shear rates would yield higher resolution patterns. Conversely, inks with a lower viscosity at low shear rates are prone to settling but tend to produce smoother surfaces due to surface tension, which minimizes the surface area.

This study aims to evaluate the feasibility of extrusion-based DW technology for creating wear sensors, while increasing sensor resolution via reduced line width and line-to-line spacing, both critical to performance. To our knowledge, this is the first study to achieve a line width of 15 μm and a line-to-line spacing of 50 μm using extrusion-based DW technology. We focus on material characterization as well as processing-structure-properties relationships in direct writing interconnects for wear-sensor applications. Furthermore, we explore the effect of process parameters on the cross-sectional profile of printed lines (Fig. 2).

2. Experimental methods

2.1. Materials

Silver is chosen as the conductive material for this application due to its high electrical conductivity (6.3×10^7 S/m [23] and wide availability as an extrusion-based DW ink. A total of five commercially available silver-based inks were studied: a silver-epoxy-based ink (Ink A; ESL1120), a silver-platinum-based ink (Ink B; ESL9595 A), a silver-based ink (Ink C; ESL9912K-FL), a silver ink designed for screen-printing (Ink D; DuPont C028), and a silver ink designed for Optomec Aerosol Jet system (Resin Design E8074). The E8074 ink was centrifuged at 4000 rpm for 20 min using Thermo Electron Corporation 8464 multi-centrifuge to create a higher viscosity "Ink E". In this study, inks were deposited onto 99% alumina plates of 0.025″ thickness.

2.2. Particle size distribution and rheological measurements

Light scattering analysis was performed using an ALV/CGS-3 compact goniometer to determine the particle size distribution. The scattering analysis assumes the particles are spherical. In a typical light scattering experiment, the ink was diluted 1 million times before measurements. Thermogravimetric analysis (TGA) was performed from 25 °C to 650 °C in nitrogen to quantify the inorganic particle content in each ink. Steady shear viscosities, small-amplitude oscillatory time sweep, and strain sweep experiments (at a fixed frequency of 0.01 Hz) were measured using an AR-G2 rheometer (TA Instruments) at 25 °C. Parallel plate fixture (diameter: 40 mm) was used with a test gap of 600 μm. For steady shear tests, viscosities were measured from high to low shear rates (from 100 s^{-1} to 0.01 s^{-1}). A strain amplitude of 0.1% and a frequency of 0.01 Hz were used for oscillatory time sweep experiments.

2.3. Direct-write printing

This study focuses on the extrusion-based DW method, which is

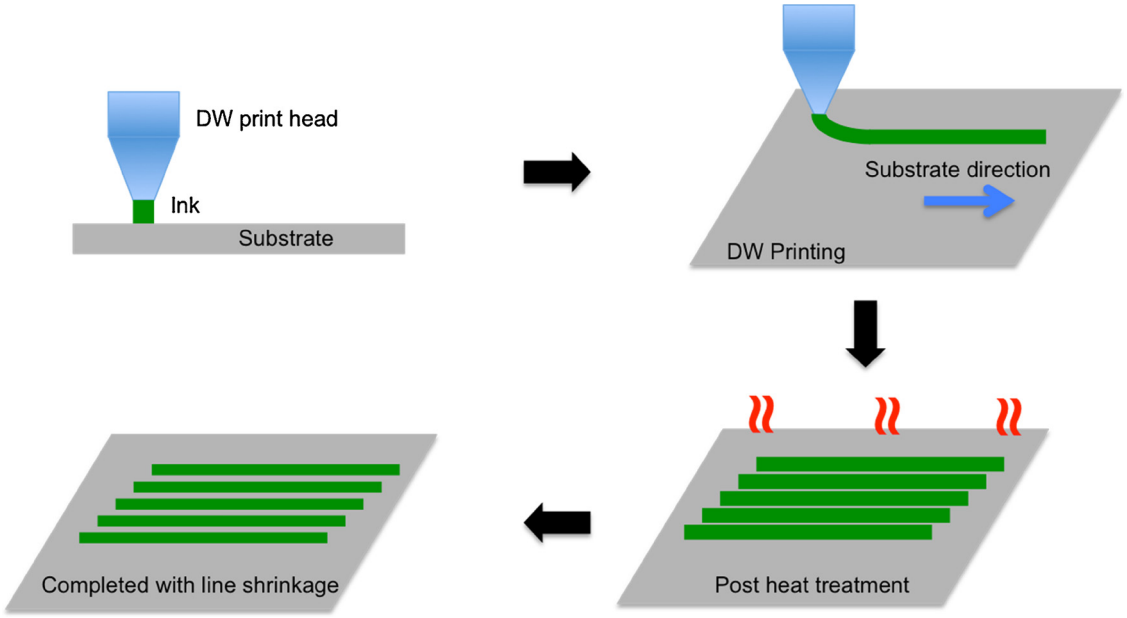

Fig. 2. Schematic diagram showing the step-by-step procedure to direct write high-density parallel interconnects.

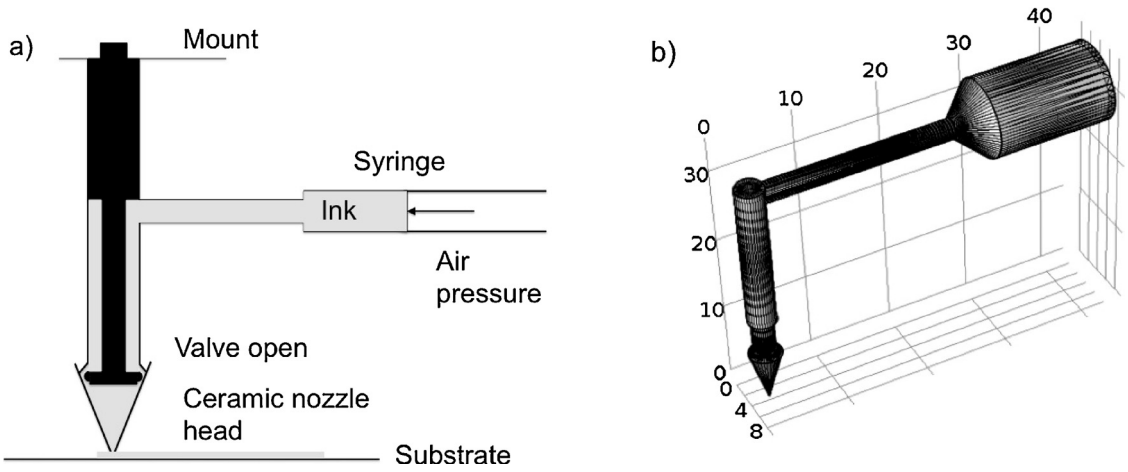

Fig. 3. a) Schematic diagram illustrating the extrusion-based DW mechanism of the n-Scrypt system. b) Control volume considered in the COMSOL simulations based on the actual geometry and dimensions of the n-Scrypt system. Valve opening is not shown, and the dimensions are in mm.

sometimes referred to as a continuous approach or a flow-based technique, commercially available from nScrypt. The nScrypt system integrates a shaft valve into the direct-print dispensing tool as illustrated in Fig. 3a. First, a 3cc syringe is loaded with the ink and connected to the assembly. When an air pressure command is sent through the software, ink fills the assembly and is stopped by a closed nozzle valve. The amount of ink extruded through the ceramic head nozzle is controlled by the degree of valve opening. A surface mapping of the substrate is performed before printing to account for any unevenness of the print surface through adjusting the height of the print head during printing. The integrated vertical valve system can dispense materials with a viscosity of up to 1000 Pa s at room temperature under controlled air pressure, valve opening, and dispensing gap [24]. One key advantage of the vertical valve system is that as the valve plunger is pulled up, a slight negative pressure is generated to pull the ink back inside the nozzle head when a deposition is finished. This feature keeps the orifice clear, reducing clogging and allowing for a good startup. A tapered nozzle is used to reduce the print line width for high resolution printing while minimizing the pressure drop. The substrate moves horizontally as print material is deposited onto the substrate for a fixed dispensing gap.

2.4. COMSOL simulations

Trial-and-error has proven to be an inefficient way to optimize process parameters for DW [25]. Due to the complicated geometry within the assembly and non-Newtonian fluid behavior, finite-element-based simulations were carried out to understand the printing process and, more specifically, to calculate the theoretical volumetric printing flow rate. Fig. 3b shows the ink fluid body inside the print head assembly. A power-law fluid model was chosen with model coefficients, namely, flow consistency index (K) and power law index (n), determined from experimental rheology data. A non-slip boundary condition at all internal walls was assumed. An inlet pressure of 40 psi, similar to experiments, was assumed. The volumetric flow rate of the ink was simulated for different valve openings. Ink density is estimated to be 4.5 g/cm^3.

2.5. Cross-sectional area measurements

Immediately after printing, the cross-sectional area of the printed silver lines was measured using a Keyence VHX-600 optical microscope. For line thicknesses less than 15 µm, a white light interferometer (Zygo

NewView 7300) measurement was also used to confirm accuracy. The total cross-sectional area is approximated by the summation of the areas of multiple slices, where the line width is multiplied by the slice thickness. Printing process was carried out at room temperature, and solvent evaporation was assumed to be negligible. Traces from the first two seconds of printing were not measured to eliminate transient effects. The experimental volumetric flow rate was estimated by multiplying the experimentally measured cross-sectional area by the set substrate translation speed. Experimental and simulated volumetric flow rates were compared to understand the impact of outside nozzle parameters (e.g., dispensing gap and substrate speed) on line definition and surface topographies.

2.6. Sintering and conductivity measurements

The printed lines were sintered following the spec sheets provided by the ink manufacturers. Inks B and C were sintered at 625 °C in air for 30 min. Inks A, D, and F were sintered at 160 °C, 150 °C, and 150 °C in air for 60 min, respectively. The electrical resistance of the sintered lines was measured using a multi-meter (LG DM-311) probe station. For each experimental condition, the resistance of a total of twenty 30-mm long silver lines was recorded. The average line resistivity and its standard deviation were calculated to assess process repeatability.

3. Experimental results and discussion

3.1. Particle size distribution and rheology results

To select an appropriate nozzle size for consistent printing, the particle size distribution of inks was characterized using light scattering. As a rule of thumb, nozzle size has to be at least 15 times larger than the largest particle size for continuous printing without clogging [17]. Fig. 4a shows the light scattering results. Of all the inks studied, Ink E has the largest average particle diameter (~1550 nm), followed by Ink A (720 nm), Ink B and Ink C (474 nm), and lastly Ink D (334 nm). The average particle size in Inks B and C is similar, but Ink B has a wider particle size distribution than that of Ink C. A small average particle size combined with a narrow size distribution generally allows the use of a small nozzle and enables uninterrupted printing without clogging. Based on the particle size analysis results, a nozzle with a 25-μm diameter was down-selected to explore printing of narrow lines, while a 75-μm nozzle diameter was used for printing actual sensors. TGA was carried out to estimate the initial solid loadings. Nitrogen gas was used to prevent silver oxidation, and the experimental results are shown in Fig. 4b. A higher solid loading is desirable because a larger amount of conductive material will remain after burning off the organic components. However, highly concentrated inks also require a higher printing pressure, and the chance of nozzle clogging increases. Of all the inks, Ink A has the lowest solid loading at only 20% by weight; whereas Ink E has the highest loading, with close to 90% of the initial mass remaining after the TGA experiment. Inks B and C have a similar loading at 86%, and Ink D has a loading of 78%. Overall, Ink C has the second highest loading, second smallest average particle size, and the narrowest distribution—all desirable qualities for printing fine conductive lines consistently.

Fig. 5 summarizes the experimental rheology data of all inks. In terms of steady shear rheology, all inks exhibited a shear-thinning behavior (i.e., viscosity decreases as the shear rate increases) within a shear-rate range of 0.01 to 100 s^{-1}. A higher viscosity at low shear rate ($\dot{\gamma} < 1\ s^{-1}$) helps retain the shape of printed patterns as the shear rate decreases after the ink exits the nozzle [5]. This is consistent with the experimental observation that Inks A and D spread to a larger extent on the substrate (due to gravity and surface wetting) compared with Inks B and C (Fig. 6). Inks B and C have better shape retention after printing. Although Ink E has the highest low-shear viscosity, it tends to clog the nozzle due to high solid loading and large particle size. A bigger nozzle with a diameter of 125 μm was used for printing Ink E. Inks B and C have similar average particle sizes and solid loadings with Ink B having a lower viscosity at low shear rates. This is attributed to the "Farris effect," which suggests a broader particle size distribution will result in a lower viscosity, because smaller particles can fill the interstitial spacing between the larger particles [26]. Ink C is the most desirable ink from a rheology perspective. Except for Ink A, all inks show no clear plateau at low or high shear rates, suggesting that the ink rheology can be described using a power-law fluid model:

$$\eta = K(\dot{\gamma})^{n-1},$$

Where η is the viscosity, K is the flow consistency index, $\dot{\gamma}$ is the shear rate, and n is the power law index. The best-fit K- and n- values for each ink are tabulated in Table 1. All n-values are smaller than 1, and the smaller the n-value, the higher degree of shear thinning.

The yield stress for the inks, defined as the shear stress at a zero shear rate, may be estimated by plotting shear stress data against shear rates, as shown in Fig. 5b. The inks in this study have an apparent yield stress ranging from nearly 0 Pa to 455 Pa, as summarized in Table 1. Caution, however, should be taken with Ink A, because no clear plateau was observed at low shear rates. The method of determining the yield stress from Fig. 5b could be compromised, because the slope of the stress-strain rate plot may change significantly below a shear rate of 0.01 s^{-1}. In addition to steady shear measurements, oscillatory shear tests were performed to determine the linear viscoelastic regime (Fig. 5c) and to measure the elastic modulus (G') as a function of time

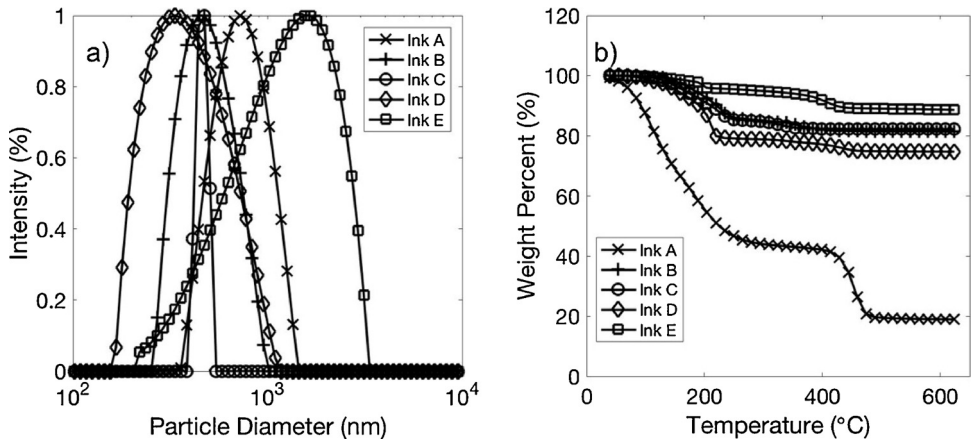

Fig. 4. a) Particle size distribution of silver particles in the five inks characterized using light scattering. b) TGA results of the five inks from 25 °C to 625 °C in nitrogen showing the difference in initial solid loading.

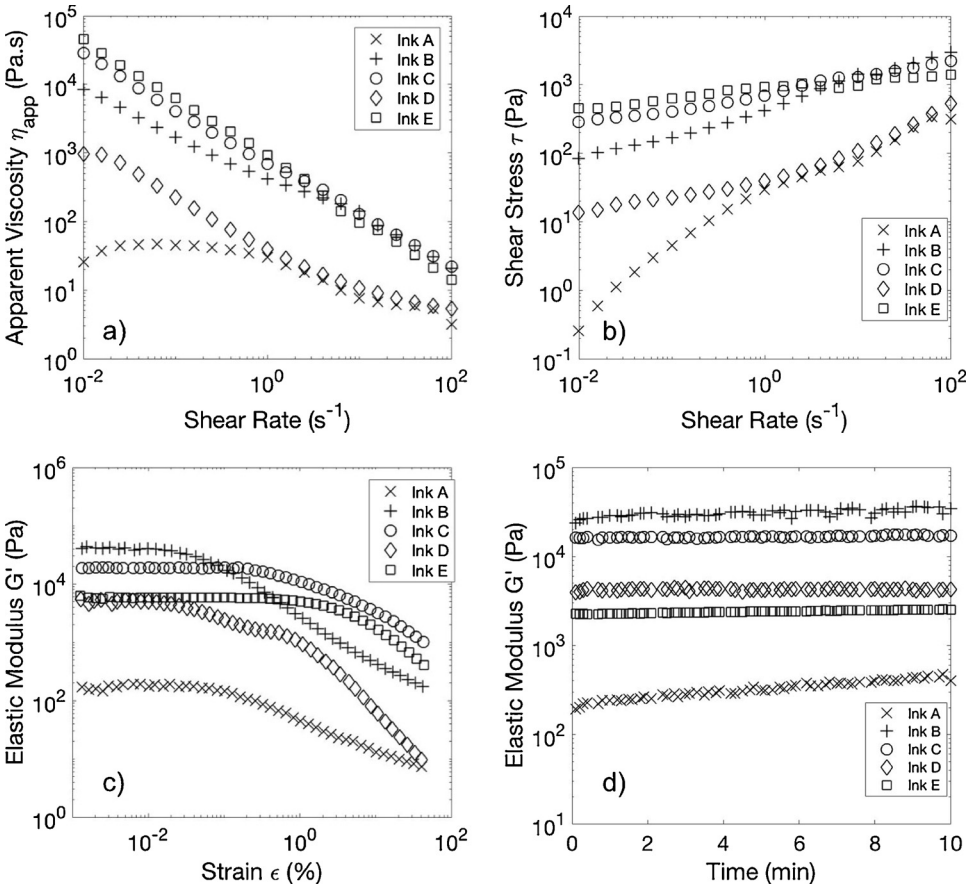

Fig. 5. a) Apparent shear viscosity as a function of shear rate measured at 25 °C. All five inks exhibit different degrees of shear-thinning behavior, and the low-shear viscosity also varies. b) A plot of shear stresses as a function of shear rates used for estimating the yield stresses for different inks at 25 °C. c) Elastic modulus (G') as a function of strain, showing non-linear behavior above a critical strain. Frequency: 1 Hz; temperature: 25 °C. d) Elastic modulus (G') as a function of time showing the time evolution and stability of the inks. Strain amplitude: 0.1%; frequency: 1 Hz.

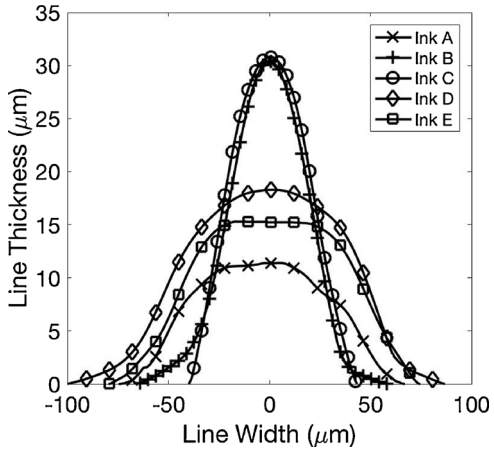

Fig. 6. Cross-sectional profile of silver inks deposited on alumina (prior to sintering), measured using a Keyence VHX-600 optical microscope. Valve opening: 0.1 mm; inlet pressure: 40 psi (except for Ink A, 15 psi was used due to the low viscosity); nozzle diameter: 75 µm (except for Ink E, a larger nozzle diameter of 125 µm was used to avoid clogging); substrate speed: 20 mm/s; dispensing gap: 50 µm.

(Fig. 5d). At small strain amplitudes, the magnitude of the elastic modulus (G') is independent of strain, as shown in Fig. 5c. However, as strain amplitude increases above a certain critical value, the modulus decreases, suggesting a strain-softening behavior. The linear viscoelastic regime is defined as the strain below this critical value, which varies from 0.013% to 0.25% for studied inks in Table 2. It is worth noting that unstable, highly flocculating suspensions tend to have a smaller critical strain [27]. From the strain sweep data, strain amplitude of 0.01% and a frequency of 0.01 Hz were identified for measurement of the elastic modulus as a function of time. As shown in Table 2, Ink C has the second highest silver loading, second smallest particle diameter, and second highest apparent viscosity at low shear (0.1 s^{-1}). Based on these results, Ink C has been further selected as the model ink for DW experiments to better understand the influence of

Table 1
The estimated silver content by weight from TGA, average particle diameter, yield stresses, and power-law fluid indices (K- and n-values) of the five inks studied. *Ink A, D, and E contain epoxy and Ink B contains platinum.

Ink name	Silver content (%)	Average particle diameter (nm)	Yield stress (Pa)	Flow consistency index K ($Pa.s^n$)	Power law index n
Ink A	20	720	N/A	18.7	0.717
Ink B	81	474	84	389	0.306
Ink C	82	474	287	711	0.207
Ink D	78	334	14	52.8	0.380
Ink E	88	1550	455	757	0.076

Table 2
Rheological properties of the DW inks: namely, apparent shear viscosity at 0.1 s^{-1} (η_{app}), critical strain, elastic modulus at different times and the corresponding percent change.

Ink name	η_{app} (Pa.s) at 0.1 s^{-1}	Linear strain regime (%)	G' (Pa) at 0 min	G' (Pa) at 10 min	% change in G'
Ink A	45.5	6.3×10^{-2}	194	404.5	108%
Ink B	1702	1.3×10^{-2}	23560	30200	28%
Ink C	4075	2.0×10^{-1}	16220	17070	5%
Ink D	227	1.6×10^{-2}	20	21.91	10%
Ink E	6285	2.5×10^{-2}	2266	2541	12%

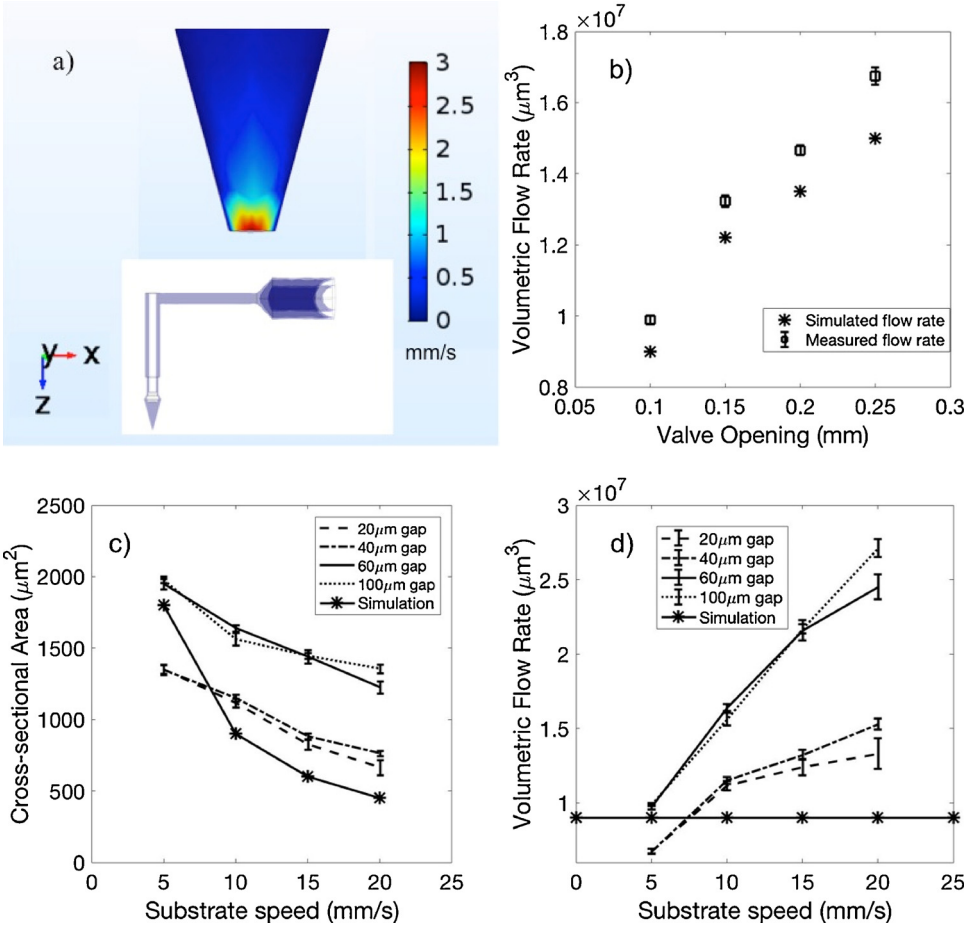

Fig. 7. a) Simulated velocity profile (in the z-direction) for Ink C with a valve opening of 0.1 mm, an inlet pressure of 40 psi, and a nozzle diameter of 75 μm. b) Comparison between the simulated volumetric flow rate (Q_s) and experimentally measured volumetric flow rate (Q_{exp}) for different valve openings. Q_{exp} was calculated from material balance by multiplying the cross-sectional area by the substrate speed. Substrate speed: 5 mm/s; dispersing gap: 200 μm. c) Cross-sectional areas of printed silver lines (pre-sintering) versus substrate speeds for different dispensing gaps ranging from 20 μm to 100 μm. Valve opening: 0.1 mm; inlet pressure: 40 psi; nozzle diameter: 75 μm. Connected lines are added to guide the eyes. d) Volumetric flow rates as a function of substrate speeds for different dispensing gaps. Valve opening: 0.1 mm; inlet pressure: 40 psi; nozzle diameter: 75 μm. Connected lines are added to guide the eyes.

printing parameters on ink volumetric flow rate and printed line topographies. Additionally, experimental results in Fig. 5c suggest all inks thicken to some extent on a time scale of 10 min, especially for Ink A where its elastic modulus doubles.

3.2. Effects of valve opening and printing speed

The printed line width depends strongly on ink rheology, as well as on printing parameters such as inlet pressure, valve opening, and the substrate's translation speed. Intuitively, narrow lines can be produced by reducing the volumetric flow rate and/or by increasing the substrate speed. As a validation, Fig. 7b compares the simulated and experimental volumetric flow rates as a function of valve opening. The experimental volumetric flow rate was estimated by multiplying the line's cross-sectional area by the translation speed. For the data in Fig. 7b, dispensing gap was set to 200 μm and substrate speed was set to 5 mm/s. As shown in the figure, a larger valve opening results in a high volumetric flow rate. This trend is in agreement with COMSOL simulations for the volumetric flow rates assuming Ink C as a power-law fluid with K = 711 Pa $s^{0.207}$ and n = 0.207 (as determined from rheology experiments in Section 3.1). However, the simulated flow rate is consistently smaller than the experimentally measured flow rate for all valve openings. Such discrepancy is probably due to: (i) possible slippage at the wall, and/or (ii) the use of a power-law fluid model, in which the apparent viscosity increases to infinity as the shear rate approaches zero, resulting in an over-estimation of viscosity at low shear rates. The end result is an under-estimation of the volumetric flow rate, as the volumetric flow rate is inversely proportional to the viscosity. Also of relevance is the fact that the simulated volumetric flow rate does not account for the effects of dispensing gap and substrate translation speed. Small dispensing gap could result in a backpressure at the nozzle tip, while high substrate speed may result in line breakage.

Fig. 7c shows the effects of substrate speed and dispensing gap on the cross-sectional area. As the translation speed of the substrate increases, the cross-sectional area decreases at a fixed flow rate. This process is analogous to the drawing process in fiber spinning [28,29]. Based on COMSOL simulations, the mean velocity at the nozzle exit is estimated to be 2.1 mm/s ($v^* = Q / A_{nozzle}$). Assuming a perfect adhesion between the printed line and the substrate, the linear translational print speed at 5, 10, 15, and 20 mm/s corresponds to a draw ratio of 2.38, 4.76, 7.14, and, 9.5, respectively. A higher draw ratio leads to a smaller cross-sectional area. In terms of gap size between the print nozzle and the substrate, the cross-sectional area decreased from 1978 μm^2 to 1351 μm^2 as the gap reduced from 100 μm to 20 μm (for a fixed print speed of 5 mm/s). This may be explained by the geometric constraints and the presence of a backpressure at the nozzle exit, as the vertical position of the substrate remains constant during printing. The inlet pressure, valve opening, dispensing gap, and print speed were varied systematically to improve the printing conditions for Ink C.

Fig. 7d compares the simulated volumetric flow rate (Q_s) with the experimentally measured volumetric flow rate (Q_{exp}) for different substrate translation speeds. At a substrate speed of 5 mm/s, Q_{exp} matches closely with Q_s for a dispensing gap of 60 μm and 100 μm; whereas Q_{exp} is smaller than Q_s for smaller dispensing gaps of 20 μm and 40 μm. At a substrate speed larger than 5 mm/s, the Q_{exp} values are larger than the simulated Q_s values. The COMSOL simulation assumes the substrate speed has no effects on the printing flow rate. However, the difference between Q_{exp} and Q_s clearly suggests the substrate has a non-negligible effect on the actual volumetric flow rate during printing. Fig. 8a illustrates different pressures or forces that may exist at the print nozzle during the printing process; namely, the pressure generated by the air pressure (P_{feed}), pressure exerted by the deposited ink due to the

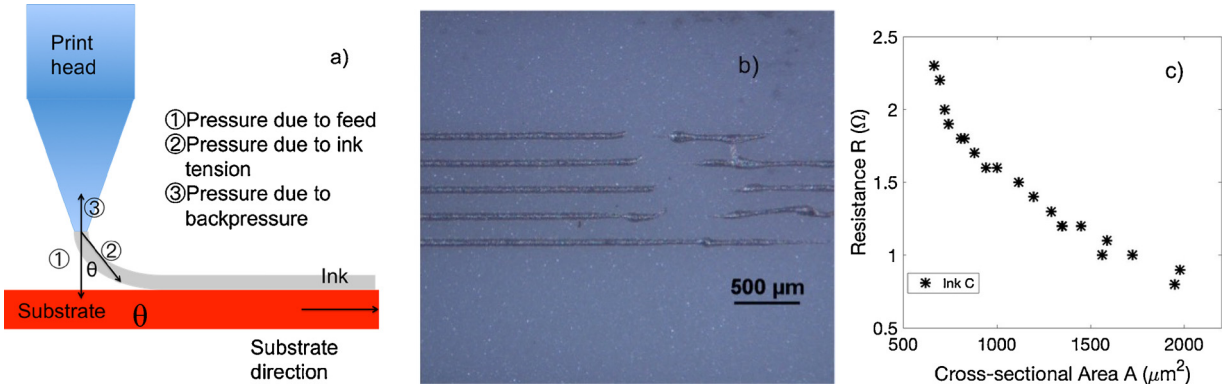

Fig. 8. a) Schematic diagram illustrating different forces or pressures at play during the DW process. The interplay of these forces has important implications on the printing flow rate, line width, and DW consistency. b) Reflected optical micrograph of DW silver lines on an alumina at exceedingly high substrate speed of 30 mm/s speed (equivalent to a draw ratio of 14). Inlet pressure: 40 psi; nozzle diameter: 75 μm; valve opening: 0.1 mm; dispensing gap: 60 μm gap. c) Measured resistance of post-sintered DW silver lines versus cross-sectional area. Line length: 30 mm; Ink C.

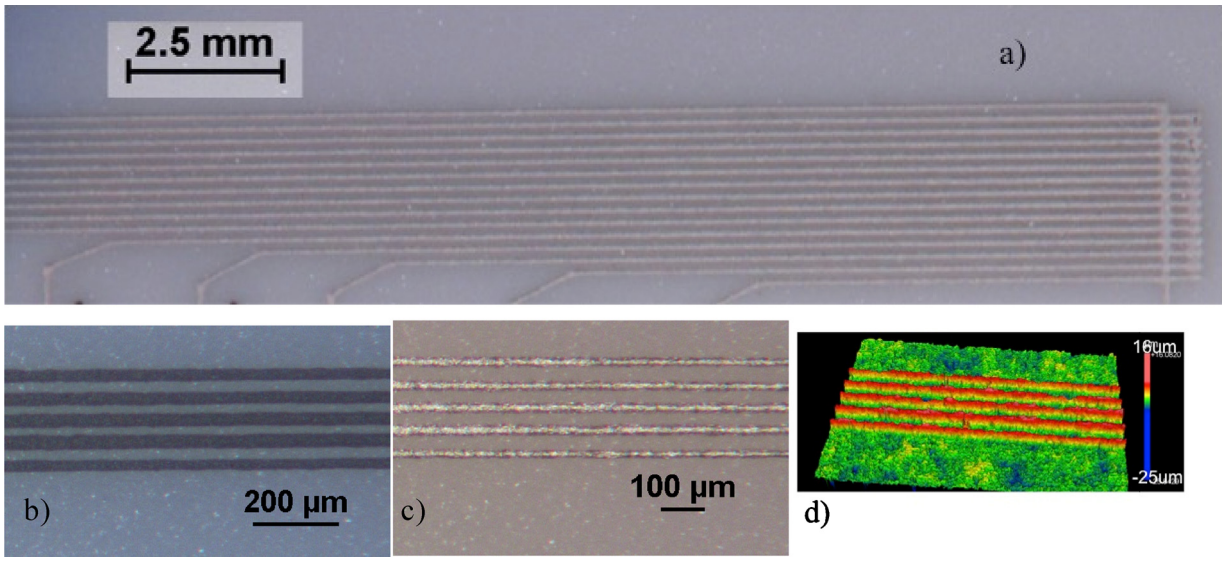

Fig. 9. a) Optical image of printed silver lines showing a ca. 150-μm center-to-center line spacing (post-sintering). Nozzle dia.: 75 μm. b) and c) are optical micrographs of silver lines with a 50 μm center-to-center line spacing, printed using a 25-μm nozzle, before and after sintering, respectively. d) 3D white light interferometry image of printed interconnect traces after sintering at 625 °C in air for 30 min. Inlet pressure: 40 psi; valve opening: 0.1 mm; dispensing gap: 60 μm; substrate speed: 30 mm/s; Ink C.

relative motion between the nozzle head and the substrate (P_{ink}), and backpressure (P_{back}). COMSOL simulations in this study only consider the flow rates induced by P_{feed}, which is the dominant pressure for large gaps and slow substrate speeds. However, P_{back} increases as a function of decreasing dispensing gap, and the presence of a backpressure would explain the smaller volumetric flow rates in the cases of 20-μm and 40-μm gaps. At high substrate translation speeds, the ink adhered to the substrate exerts a force pulling on the ink at the nozzle and consequently leading to a higher flow rate. Similar behavior has been documented in the polymer fiber spinning literature [26,30,31] The magnitude of force depends on the dispensing gap, which changes the angle of extrusion, as well as the rheology or "stretchability" of the ink. The force is advantageous for reducing the cross-sectional area as discussed previously, but exceedingly high substrate speed will also result in instability and possible ink fracture, as evidenced in Fig. 8b. Our experimental findings suggest the best dispensing gap for printing narrow lines is around 60–70% of the nozzle diameter. Narrowest lines in this study were obtained using a 25-μm diameter nozzle, an inlet pressure of 40 psi, a valve opening of 0.1 mm, a dispensing gap of 20 μm, and a substrate speed of 20 mm/s. The full set of experimental data is included in Supporting Information for completeness.

3.3. Printed structure characterization

The electrical resistance of the sintered silver lines was measured at room temperature as shown in Fig. 8c as a function of cross-sectional area for 30-mm lines. Bulk resistivity of the lines was then calculated from this data. An average electrical resistivity of 5.29×10^{-8} Ω·m (about three times the literature value of bulk silver resistivity [21]) with a standard deviation of 3.68×10^{-9} Ω·m was achieved. The high conductivity of printed silver traces enables high accuracy and reliability of sensors. Fig. 9a shows a 2D optical image of DW silver lines after sintering. A center-to-center line spacing of 150 μm was specified in the design, and an actual line width of 95 μm was achieved post-sintering with a 75-μm inner diameter nozzle. The closest distance between the lines is on the order of 15 μm. Subsequent electrical measurements showed no apparent signs of shorts between the parallel lines. A smaller 25 μm diameter nozzle has additionally been utilized to print narrower lines. Figs. 9b and c show optical images of the printed lines before and after sintering, respectively. The as-printed line width is ca. 26 μm and shrunk to about 15 μm after sintering. The measured average center-to-center line spacing is about 50 μm. Small line-spacing enables high resolution sensing during wear events. Line thickness was

measured to be 12 µm before sintering and 8 µm after sintering (Fig. 9d).

4. Conclusions

This study demonstrates feasibility of the extrusion-based DW method for creating high-density silver lines for wear-sensor applications. We characterized five commercially available silver inks for rheology and particle size distribution and chose Ink C for its relatively high silver loading, low-shear viscosity, small particle size, and narrow particle size distribution. We used COMSOL to simulate volumetric flow rates during the DW process, assuming Ink C as a power-law fluid, and compared simulated versus experimentally measured volumetric flow rates at different valve openings, dispensing gaps, and substrate speeds. Our simulations accurately predicted experimental results, showing larger valve openings led to larger volumetric flow rates. Simulated flow rates, however, proved consistently smaller than those observed experimentally, likely due to assuming a power-law fluid and non-slip boundary conditions. Our tests of different substrate translation speeds showed higher speeds resulted in printed lines with smaller cross-sectional areas, a trend successfully captured by our COMSOL simulations. Increases in substrate speed also correlated with increases in volumetric flow rates, possibly due to tension exerted by the printed lines adhered to the substrate. Extremely high substrate speed resulted in ink fracture and discontinued lines due to the increase in force exerted on ink in air by ink adhered to the substrate. A small dispensing gap of about 50% of print nozzle diameter created backpressure close to the nozzle and thus reduced printing flow rates. In summary, we conclude a small gap and high substrate speed are desirable for printing high density interconnects. Using the chosen ink and a 25-µm nozzle, we achieved 15-µm silver lines with a line spacing of 50 µm.

Acknowledgements

The team acknowledges financial support from United Technologies Research Center (UTRC), Connecticut Space Grant Consortium, and Anton Paar Research Fellowship.

Appendix A. Supplementary data

Supplementary material related to this article can be found, in the online version, at doi: https://doi.org/10.1016/j.addma.2018.05.010.

References

[1] M. Federici, C. Menapace, A. Moscatelli, S. Gialanella, G. Straffelini, Effect of roughness on the wear behavior of HVOF coatings dry sliding against a friction material, Wear 368–369 (2016) 326–334, http://dx.doi.org/10.1016/j.wear.2016.10.013.
[2] T. Dyck, P. Ober-Wörder, A. Bund, Calculation of the wear surface and the coefficient of friction for various coated contact geometries, Wear 368–369 (2016) 390–399, http://dx.doi.org/10.1016/j.wear.2016.10.014.
[3] J.A. Lewis, Direct ink writing of 3D functional materials, Adv. Funct. Mater. 16 (17) (2006) 2193–2204, http://dx.doi.org/10.1002/adfm.200600434.
[4] A. Shen, C.P. Bailey, A.W.K. Ma, S. Dardona, UV-assisted Direct Write of Polymer bonded Magnets, J. Magn. Magn. Mater. 462 (2018) 220–225, http://dx.doi.org/10.1016/j.jmmm.2018.03.073.
[5] J.A. Lewis, G.M. Gratson, Direct writing in three dimensions, Mater. Today 7 (7) (2004) 32–39, http://dx.doi.org/10.1016/S1369-7021(04)00344-X.
[6] S.R. Culp, S. Dardona, W.R. Schmidt, Method for manufacturing layered electronic devices. US Patent 9,832,875.
[7] S. Dardona, P. Sheedy, M. Piech, D.A. Grande, W.R. Schmidt, C. Tokgoz, T.D. Kasprow, L.V. Protsilo, Embeded sensor for in-situ monitoring of blade tip incusion. US Patent 9,939,247.
[8] S. Dardona, J. Hoey, Y. She, W.R. Schmidt, Direct write of copper-graphene composite using micro-cold spray, AIP Adv. 6 (8) (2016), http://dx.doi.org/10.1063/1.4961510.
[9] V.K. Lee, G. Dai, Three-dimensional bioprinting and tissue fabrication: prospects for drug discovery and regenerative medicine, Adv. Health Care Technol. 1 (2015) 23–35, http://dx.doi.org/10.2147/AHCT.S69191.
[10] S. Dardona, A. SHen, C. Tokgoz, Direct write fabrication of a wear sensor, IEEE Sens. J. 18 (8) (2018) 3461–3466 10.1109/JSEN.2018.2810839.
[11] W.J. Hyun, E.B. Secor, M.C. Hersam, C.D. Frisbie, L.F. Francis, High-resolution patterning of graphene by screen printing with a silicon stencil for highly flexible printed electronics, Adv. Mater. 27 (1) (2015) 109–115, http://dx.doi.org/10.1002/adma.201404133.
[12] O. Krammer, L.M. Molnár, L. Jakab, A. Szabó, Modelling the effect of uneven PWB surface on stencil bending during stencil printing process, Microelectron. Reliab. 52 (1) (2012) 235–240, http://dx.doi.org/10.1016/j.microrel.2011.08.012.
[13] GyslingHJ, Nanoinks in inkjet metallization—evolution of simple additive-type metal patterning, Curr. Opin. Colloid Interface Sci. 19 (2014) 155–162.
[14] B.E. Kahn, The M3D aerosol jet system, an alternative to inkjet printing for printed electronics, Org. Print. Electron. 1 (2007) 14–17.
[15] E. Jabari, E. Toyserkani, Micro-scale aerosol-jet printing of graphene interconnects, Carbohydrate Res. 91 (27) (2015) 321–329, http://dx.doi.org/10.1016/j.carbon.2015.04.094.
[16] B.B. Li, P.A. Clark, K.H. Church, ASME. International Manufacturing Science and Engineering Conference, ASME 2007 International Manufacturing Science and Engineering Conference, Robust Direct-Write Dispensing Tool and Solutions for Micro/Meso-Scale Manufacturing and Packaging (2018) 715–721, http://dx.doi.org/10.1115/MSEC2007-31037.
[17] J. Palmer, (2008). Methods and Systems for Rapid Prototyping of High Density Circuits. U.S. Patent.
[18] K.B. Perez, C.B. Williams, Combining additive manufacturing and direct write for integrated electronics – a review, International Solid Freeform Fabrication Symposium Proceedings, (2013), pp. 962–979.
[19] S.L. Morissette, J.A. Lewis, P.G. Clem, J. Cesarano, D.B. Dimos, Direct-write fabrication of Pb(Nb,Zr,Ti)O 3 devices: influence of paste rheology on print morphology and component properties, J. Am. Ceram. Soc. 84 (11) (2001) 2462–2468, http://dx.doi.org/10.1111/j.1151-2916.2001.tb01036.x.
[20] K. Sun, T.S. Wei, B.Y. Ahn, J.Y. Seo, S.J. Dillon, J.A. Lewis, 3D printing of interdigitated Li-ion microbattery architectures, Adv. Mater. 25 (33) (2013) 4539–4543.
[21] B. Li, P.A. Clark, K.H. Church, Robust direct-write dispensing tool and solutions for Micro/Meso-scale manufacturing and packaging, Proceedings of the ASME International Manufacturing Science and Engineering Conference, (2007).
[22] R. Rellán-Álvarez, G. Lobet, J.R. Dinneny, Multiscale modeling of powder bed–based additive manufacturing, Annu. Rev. Mater. Res. 46 (2016) 1–34, http://dx.doi.org/10.1146/annurev-matsci-070115-032158 (August).
[23] Raymond A. Serway, Principles of Physics, 2nd ed., Saunders College Pub., Fort Worth, Texas; London, 1998, p. 602 ISBN 0-03-020457-7.
[24] B. Li, P.A. Clark, K.H. Church, Robust direct-write dispensing tool and solutions for Micro/Meso-scale manufacturing and packaging, Proceedings of the ASME International Manufacturing Science and Engineering Conference, (2007).
[25] R. Rellán-Álvarez, G. Lobet, J.R. Dinneny, Multiscale modeling of powder bed–based additive manufacturing, Annu. Rev. Mater. Res. 46 (2016) 1–34, http://dx.doi.org/10.1146/annurev-matsci-070115-032158 (August).
[26] N.K.O. Ojijo, E. Shimoni, Minimization of cassava paste flow properties using the “Farris effect, LWT – Food Sci. Technol. 41 (1) (2008) 51–57, http://dx.doi.org/10.1016/j.lwt.2007.01.020.
[27] M. Castro, D.W. Giles, C.W. Macosko, T. Moaddel, Comparison of methods to measure yield stress of soft solids, J. Rheol. 54 (1) (2010) 81, http://dx.doi.org/10.1122/1.3248001.
[28] B. Younes, A. Fotheringham, H.M. EL-Dessouky, G. Haddad, Factorial optimization of the effects of melt-spinning conditions on As-spun aliphatic-aromatic copolyester fibers I. Spin draw ratio, overall orientation and drawability, Int. J. Polym. Mater. 60 (5) (2011) 316–339, http://dx.doi.org/10.1080/00914037.2010.531804.
[29] W. Hoogsteen, R.J. van der Hooft, A.R. Postema, G. ten Brinke, A.J. Pennings, Gel-spun polyethylene fibres, J. Mater. Sci. 23 (1988) 3467–3474, http://dx.doi.org/10.1007/BF00540480.
[30] S. Zargham, S. Bazgir, A. Tavakoli, A.S. Rashidi, R. Damerchely, The effect of flow rate on morphology and deposition Area of electrospun nylon 6 nanofiber, J. Eng. Fibers Fabrics 7 (4) (2012) 42–49.
[31] W.H. Kohler, A.J. McHugh, 2D modeling of high-speed fiber spinning with flow-enhanced crystallization, J. Rheol. 51 (4) (2007) 721, http://dx.doi.org/10.1122/1.2736399.